Analytical Methods

PAPER

View Article Online
View Journal | View Issue

Metal organic framework-derived anthill-like Cu@carbon nanocomposites for nonenzymatic glucose sensor

Cite this: *Anal. Methods*, 2014, **6**, 1550

Changting Wei,[a] Xia Li,[a] Fugang Xu,[a] Hongliang Tan,[a] Zhuang Li,[b] Lanlan Sun[c] and Yonghai Song*[a]

A novel nonenzymatic glucose sensor was constructed based on anthill-like Cu@carbon nanocomposites which were derived from a Cu-based metal organic framework by a simple thermolysis method. The final nanocomposites were characterized by scanning electron microscopy, thermogravimetric analysis, X-ray powder diffraction and electrochemical techniques. The results showed that the derived nanocomposites maintained the morphology of the original materials upon thermolysis, while the produced Cu nanoclusters were embedded in three-dimensional carbon frameworks and presented an anthill-like structure. Since the final products gave a sufficiently large specific surface area, good catalytic activity towards the oxidation of glucose and appropriate pores for electrolyte transfer, the resultant glucose sensor based on the anthill-like Cu@carbon nanocomposites showed a wide linear range of 0.2–8.0 mM and a low detection limit of 29.8 μM. The low cost, simple preparation and good catalytic activity of anthill-like Cu@carbon nanocomposites render them promising candidates as electrode materials for the construction of novel nonenzymatic sensors.

Received 9th October 2013
Accepted 11th December 2013

DOI: 10.1039/c3ay41764f

www.rsc.org/methods

1. Introduction

Some chronic illnesses such as diabetes, obesity, hypertension, high cholesterol and cardiovascular diseases are now leading causes of death, which may be related to high levels of glucose in the blood. Glucose is one of the substances necessary for life, and it can be ingested directly and produced in metabolic processes to provide energy to maintain normal life activities.[1,2] Therefore, quantitative determination of glucose, both in blood and other sources such as foods and pharmaceuticals, is very important in clinical analysis.[3,4]

In recent years, many novel nanomaterials, including carbon-based materials, metals and metal oxides, have been used to fabricate simple, convenient nonenzymatic glucose sensors owing to their large specific surface areas, good stability and catalytic activity.[5,6] Cu or Cu_xO nanostructures, unlike precious metals (*e.g.* Pt, Au),[7] are important materials which are non-toxic and low in price. When compared with other common metal nanomaterials (*e.g.* Ni, Co),[8–10] Cu or Cu_xO nanomaterials always show higher catalytic activity. They have recently naturally triggered one category of nonenzymatic sensor.[11–13] Since nanomaterial aggregation might decrease the catalytic activity and specific surface area, well-dispersed Cu nanomaterials are desired. Some carbon materials with large surface areas, such as graphene,[14,15] carbon nanotubes (CNTs),[16] *etc.*, have been introduced as matrices to load Cu or Cu_xO to enlarge the effective area and improve catalytic activity and dispersion. However, preparation of the matrix and the loading steps of Cu or Cu_xO are troublesome. Recently, metal organic frameworks (MOFs) have been used as an available matrix to load a series of metal nanoparticles and proteins.[17,18] MOFs have received considerable attention, not only for their three-dimensional (3D), infinitely extended structures but also for their unique properties as highly tailorable microporous materials. They are composed of repeated metal complex units and organic ligands, which makes it possible to design various MOF structures.[19] In addition, MOFs have been converted into 3D porous carbon materials or metal (metal oxide)@carbon nanocomposites by a simple thermolysis method[20,21] for supercapacitors and lithium ion batteries. For example, MOF-derived porous carbons can be used as excellent electrode materials for electrochemical double-layered capacitors.[22] Similarly, MOF-derived metal (or metal oxide)@carbon nanocomposites might be used as advanced electrode materials to construct electrochemical nonenzymatic sensors, where carbon acts as a matrix to load metal nanoparticles. However, as far as we know, there have been no reports on the use of MOF-derived materials in electrochemical sensors.

[a]*Key Laboratory of Chemical Biology, Key Laboratory of Functional Small Organic Molecules, Ministry of Education, College of Chemistry and Chemical Engineering, Jiangxi Normal University, Nanchang 330022, Jiangxi Province, China. E-mail: yhsonggroup@hotmail.com; Fax: +86 791 8120862; Tel: +86 791 8120862*

[b]*State Key Laboratory of Electroanalytical Chemistry, Changchun Institute of Applied Chemistry, Chinese Academy of Sciences, Changchun 130022, China*

[c]*State Key Laboratory of Luminescence and Applications, Changchun Institute of Optics, Fine Mechanics and Physics, Chinese Academy of Sciences, 3888 East Nan-Hu Road, Changchun 130033, China*

Here, HKUST-1 [$Cu_3(BTC)_2 \cdot 3H_2O$; where BTC is 1,3,5-benzenetricarboxylic acid] was used to produce 3D anthill-like Cu@carbon nanocomposites by simple thermolysis. A novel nonenzymatic glucose sensor based on the anthill-like Cu@carbon nanocomposites was developed. HKUST-1 is one of the most representative MOFs, known for its unique interconnected [$Cu_2(O_2CR)_4$] paddle-wheel units which create a 3D system of channels.[23,24] By thermolysis, multipodal rigid organic linkers in HKUST-1 can be transformed into a carbon framework which can act as a matrix, and Cu^{2+} can form Cu nanoclusters embedded in the carbon frameworks. The Cu@carbon nanocomposite modified electrode showed good electrocatalytic ability towards the oxidation of glucose. The experimental conditions relating to the preparation of the Cu@carbon nanocomposites, as well as the modified electrode, and the performance of the resultant sensor, were investigated in detail.

2. Experimental section

2.1 Chemicals and reagents

1,3,5-Benzenetricarboxylic acid (BTC) was obtained from Sigma-Aldrich (Milwaukee, Wisconsin). $Cu(NO_3)_2 \cdot 3H_2O$ (99.5%), NaOH (96%), NaCl (99%), KCl (≥99.5%), KNO_3 (99%), Na_2SO_4 (≥99%), $NaNO_2$ (≥99%) and glucose were purchased from Beijing Chemical Reagent Factory (Beijing, China). All reagents were of analytical grade and used as received. All solutions were prepared with ultra-pure water, purified by a Millipore-Q system (18.2 MΩ cm).

2.2 Preparation of HKUST-1

HKUST-1 was synthesized according to the literature.[24] Briefly, 0.875 g (3.6 mmol) $Cu(NO_3)_2 \cdot 3H_2O$ was dissolved in 12 mL ultra-pure water, while 0.42 g (2.0 mmol) BTC was dissolved in 12 mL ethanol. The two solutions were mixed in equal volume, and then the mixed solution was transferred into a Teflon reaction kettle, placed in an autoclave, and heated to 393 K for 12 h. Finally, the crude product was washed with an ethanol–water mixture (volume ratio 1 : 1) several times and then dried at room temperature.

2.3 Preparation of anthill-like Cu@carbon nanocomposites

HKUST-1 was placed in a ceramic boat and was then transferred into a horizontal quartz tube and calcined in the horizontal tube furnace. The thermolysis was performed under a N_2 atmosphere with a heating rate of 5 °C min^{-1} from room temperature to 800 °C, followed by natural cooling to room temperature (denoted as Cu@C_{800}). To study the effect of the carbonization temperature, similar experiments were carried out at different target temperatures to obtain Cu@C_{400} and Cu@C_{600} nanocomposites. In addition, Cu@$C_{800\text{-}2H}$ and Cu@$C_{800\text{-}8H}$ nanocomposites were also prepared to investigate the effect of the carbonization time. The Cu@$C_{800\text{-}2H}$ and Cu@$C_{800\text{-}8H}$ nanocomposites were obtained by pyrolyzing HKUST-1 under a N_2 atmosphere with a heating rate of 5 °C min^{-1} from room temperature to 800 °C, and maintained for 2 h and 8 h before cooling, respectively.

2.4 Preparation of Cu@carbon nanocomposite modified electrode

A glassy carbon electrode (GCE) was carefully polished with 1.0 and 0.3 μm Al_2O_3 powder in turn, and then rinsed thoroughly with ultra-pure water and ethanol and dried with N_2. Simultaneously, 1.0 mg HKUST-1-derived anthill-like Cu@carbon nanocomposites were dispersed into 1.0 mL ultra-pure water to give 1.0 mg mL^{-1} homogeneous dispersions. Then, 9.0 μL suspension was dropped on the polished GCE surface and dried in air. Finally, 1.0 μL 0.5% Nafion was cast onto the modified electrode surface and then dried at room temperature.

2.5 Apparatus

Scanning electron microscopy (SEM) images were taken using an XL30 ESEM-FEG SEM at an accelerating voltage of 20 kV to study the product morphology. X-ray powder diffraction (XRD) data were collected on a D/Max 2500 V/PC X-ray powder diffractometer using Cu Kα radiation (λ = 1.54056 Å, 40 kV, 200 mA). Thermogravimetric analysis (TGA) was conducted under a N_2 flow with a heating rate of 5 °C min^{-1}, using an SDT 2960 instrument. Nitrogen isotherms were measured at −196 °C using an ASAP 2020 instrument (Micromeritics). Before the experiments, the samples were outgassed under vacuum at 120 °C. The surface area, the micropore volume, the mesopore volume and the total pore volume were calculated from the isotherms.

All electrochemical measurements were performed on a CHI 660C electrochemical workstation (Shanghai, China) at ambient temperature. A conventional three-electrode system was employed including a bare or modified GCE as the working electrode, a platinum wire as the auxiliary electrode and an SCE (saturated calomel electrode) as the reference electrode. The cyclic voltammetry experiments were performed in a quiescent solution. The amperometric experiments were carried out under continuous stirring using a magnetic stirrer, apart from the chronoamperometry experiments used for evaluation of the catalytic rate constant K_{cat}. 0.1 M NaOH was used as the supporting electrolyte solution and was purged with high purity N_2 for 15 min prior to measurements; a N_2 atmosphere was then maintained over the solution during measurements.

3. Results and discussion

3.1 Characteristics of HKUST-1

Since HKUST-1 was first reported in 1999,[23] it has been prepared by a number of methods, including microwave irradiation,[25] ultrasonic synthesis,[26] electrochemical synthesis,[27] *etc.* As can be seen from Fig. 1A and B, the HKUST-1 prepared in our work has a typical octahedral structure with a smooth surface. The X-ray diffraction pattern of the as-prepared HKUST-1, shown in Fig. 1C, was consistent with previous results.[24] Fig. 1D showed TGA of HKUST-1 in a N_2 atmosphere with a heating rate of 5 °C min^{-1}. As reported previously,[20] the framework was stable up to 300 °C. The first main weight loss stage was due to the dehydration of the material up to 100 °C. The second stage, from 300 °C to 350 °C, was mainly caused by the decomposition of the

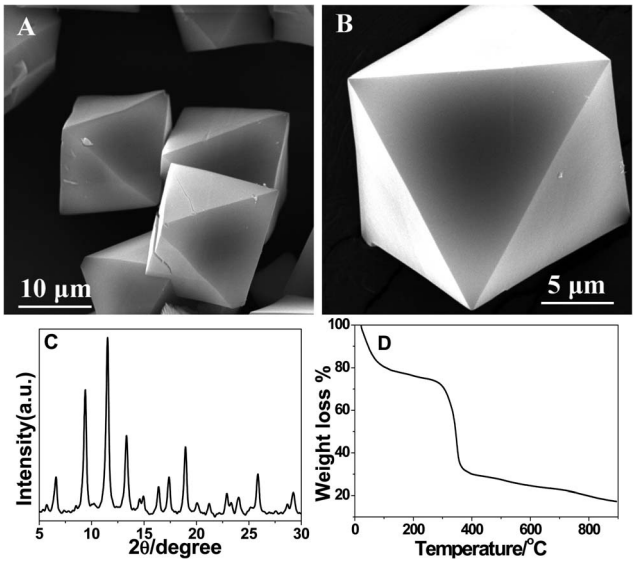

Fig. 1 Low-magnification (A) and high-magnification (B) SEM images, XRD pattern (C) and TGA (D) of as-prepared HKUST-1.

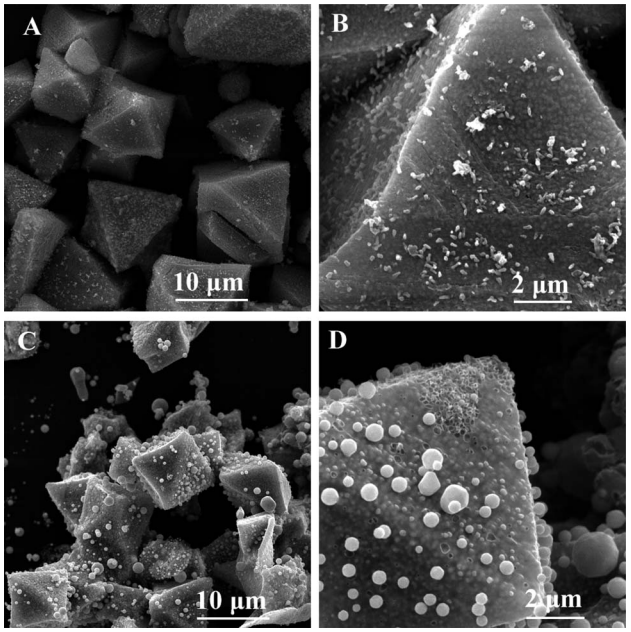

Fig. 2 Low-magnification (A and C) and high-magnification (B and D) SEM images of Cu@C_{400} (A and B) and Cu@C_{800} (C and D).

framework and evolution of CO and CO_2. Because of the lack of sufficient oxygen, the weight loss was significantly lower than expected for a complete transformation into CO_2 and Cu nanocomposites.

3.2 HKUST-1-derived anthill-like Cu@carbon nanocomposites

The morphologies of various anthill-like Cu@carbon nanocomposites derived under different conditions were studied by SEM. In all cases, the resultant materials maintained the original morphology of HKUST-1. For Cu@C_{400}, as shown in Fig. 2A and B, the octahedron framework surface was sparsely decorated with sesame-like particles and there were also looming particles embedded in the octahedral framework. As the temperature and carbonization time increased, more and more particles appeared, while small particles agglomerated into larger ones. At 800 °C, as seasame-like particles agglomerated and converted into spheres, the material presented an anthill-like structure, as shown in Fig. 2C and D. Several scattered particles might be caused by outer surface decomposition. As the carbonization time at 800 °C increased, more and more particles appeared on the surface of Cu@C_{800} (Fig. 3A and C). The high-magnification SEM images showed that the particles became larger (Fig. 3B and D).

The crystal structure was investigated by XRD. In Fig. 4A, three sharp peaks at $2\theta = 44°$, 51° and 74° in all XRD patterns match well with the (111), (200), and (220) crystal planes of the pure solid copper phase (PDF card no. 04-0836). In addition, an obscure broad peak at $2\theta = 20°$ corresponding to the carbon (002) diffractions was also observed. This result indicated that Cu@C nanocomposites were successfully prepared by thermolysis. For the metal and metal oxides derived by the thermolysis of MOFs, there is an interesting regularity. A broad range of metal and metal oxides embedded in a carbon matrix, such as Cu/CuO, Co/Co_3O_4, ZnO, Mn_2O_3, MgO and CdS/CdO, derived by thermolysis of MOFs, has demonstrated that metal ions with a reduction potential of −0.27 V or higher present in MOFs always form pure metal NPs during thermolysis in N_2, whereas metal ions with a reduction potential lower than −0.27 V form metal oxides during thermolysis in N_2.[17] Cu^{2+} is a strong oxidizing agent with a reduction potential higher than −0.27 V. When thermolysis was performed in N_2, it formed pure metal nanoparticles.[17] The three sharp peaks at $2\theta = 44°$, 51° and 74° gradually became narrow as the temperature and carbonization time increased. According to XRD patterns, the average grain size of Cu nanostructures can be calculated by the Scherrer formula[28] to be about 31.3 nm, 33.5 nm, 46.9 nm, 52.2 nm and 59.9 nm for Cu@C_{400}, Cu@C_{600}, Cu@C_{800}, Cu@$C_{800\text{-}2H}$ and Cu@$C_{800\text{-}8H}$, respectively. The Scherrer formula is applied assuming that the diffraction broadening results only from the size of the coherently scattering domains, neglecting the experimental broadening and contribution of strain.

N_2 adsorption–desorption isotherms were obtained to measure the surface area and the pore size distribution of the resultant Cu@C materials. As shown in Fig. 4B and C and Table 1, as the temperature and carbonization time increased, the volumes of micropores, mesopores and macropores varied gradually. The micropores might initially arise from the channels or pores of HKUST-1, and the mesopores and macropores might result when the Cu nanoparticles became detached from HKUST-1-derived anthill-like Cu@carbon nanocomposites. The decrease in micropores should result in a decrease of the specific surface area, but the formation of HKUST-1-derived anthill-like Cu@carbon nanocomposites with nano-sized Cu nanoparticles would enlarge the specific surface area. Therefore, the Cu@C_{600} showed the highest specific area among

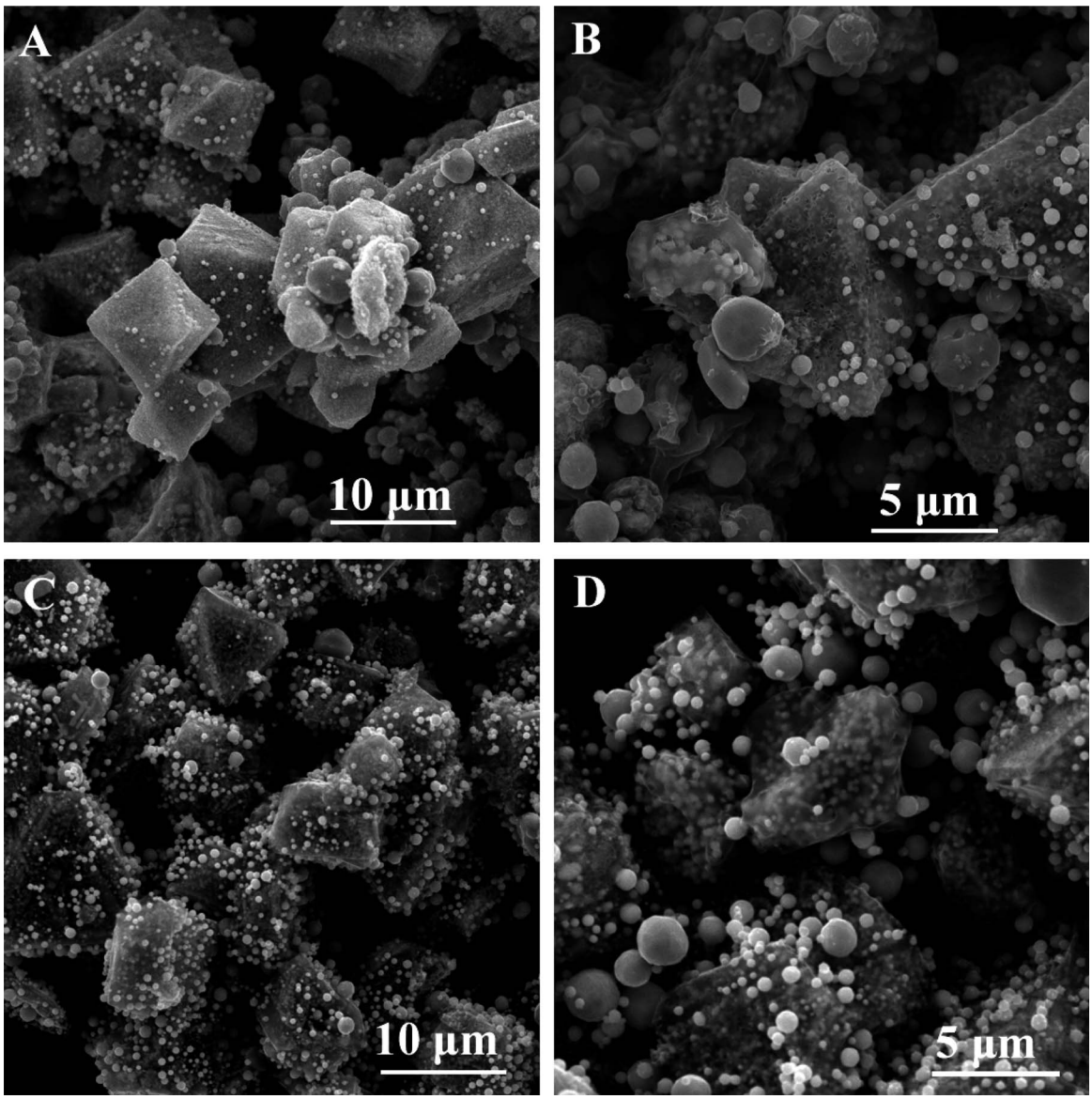

Fig. 3 Low-magnification (A and C) and high-magnification (B and D) SEM images of Cu@$C_{800\text{-}2H}$ (A and B) and Cu@$C_{800\text{-}8H}$ (C and D).

these Cu@C materials, as shown in Table 1. As the temperature further increased, a decreased surface area was found in Cu@C_{800}, owing to the disappearance of micropores and an increase in average grain size of the Cu nanoparticles. Although some micropores were reformed as the carbonization time increased,[29] the rapid aggregation of Cu nanoparticles might result in a decreased surface area of Cu@$C_{800\text{-}2H}$, as shown in Table 1. As the carbonization time further increased, a rapid increase in micropores led to an increased surface area of Cu@$C_{800\text{-}8H}$.

3.3 Electrocatalytic oxidation of glucose at the Cu@C modified electrode

Taking Cu@C_{800} as an example, the electrochemical behavior of the Cu@C_{800} modified electrode was investigated by CVs at different scan rates in 0.1 M NaOH solution, as shown in Fig. 5A. It was obvious that the current was enhanced and the reduction potential shifted negatively with an increase in scan rate. The currents measured at 0.55 V *vs.* SCE are proportional to the square root of the scan rate from 50 mV s^{-1} to 500 mV s^{-1} (Fig. 5B), indicating that the electron transfer reaction involved a diffusion-confined process. According to the above CV results and previous conclusions, the possible redox mechanism can be assumed to be as follows:[30]

$$Cu(0) + 2OH^- \leftrightarrow Cu(OH)_2 + 2e^- \quad (1)$$

$$Cu(OH)_2 + OH^- \leftrightarrow CuOOH + H_2O + e^- \quad (2)$$

Firstly, the Cu(0) was transformed into $Cu(OH)_2$ under alkaline conditions, and was then further oxidized to CuOOH as the potential shifted in the positive direction. CuOOH can be

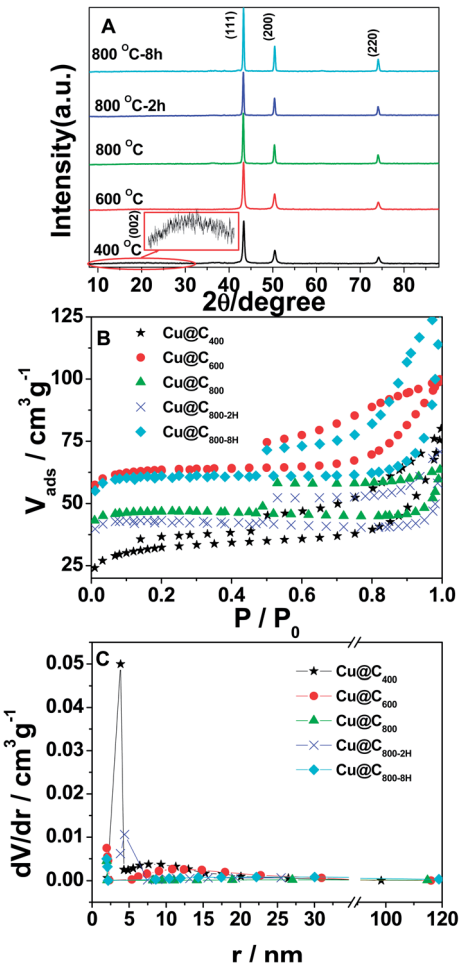

Fig. 4 XRD patterns and a partially enlarged image (A), nitrogen adsorption–desorption isotherms (B) and pore size distributions (C) of Cu@C materials.

used as a heterogeneous catalyst, and has shown good chemical stability and electrocatalytic activity.[2,30] As mentioned above, the redox process of $Cu(OH)_2$ was accompanied by the transfer of OH^-. Thus, the slow diffusion of OH^- might control the electrochemical process and result in the linear dependence of the peak current on the square root of the scan rate. The oxidation of $Cu(OH)_2$ was accompanied by the oxidation of H_2O, and accordingly an obvious oxidation peak could not be observed.

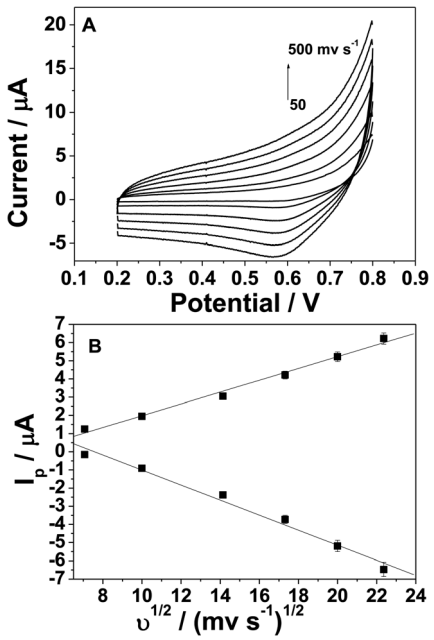

Fig. 5 (A) CVs of the Cu@C_{800} modified electrode in 0.1 M NaOH solution at various scan rates: 20, 50, 100, 200, 300, 400 and 500 mV s^{-1}. (B) Plot of peak current (at 0.5 V) *versus* the square root of the scan rate.

The electrocatalytic activity of the Cu@C_{800} modified electrode towards the oxidation of glucose was investigated using CVs in 0.1 M NaOH. As shown in Fig. 6A, the Cu@C_{800} modified electrode showed an obvious catalytic oxidation current with the addition of glucose. As a comparison, the electrocatalytic activities of Cu@C modified electrodes were also investigated, as shown in Fig. 6B. The catalytic oxidation current of the Cu@C_{800} modified electrode towards the oxidation of glucose was the highest among these Cu@C modified electrodes. This might be ascribed to the small pore size and Cu nanoparticle size in the nanocomposites. At 600 °C, mesopores and macropores had newly appeared.[29] Compared with Cu@C_{800}, a narrow pore distribution and only a few suitable pores for electrolyte and glucose transfer might result in poor catalytic activity of Cu@C_{600}, regardless of the small Cu nanoparticles. A further increase in temperature transformed the product into a more porous material, especially with regards to mesopores and macropores. Compared with Cu@C_{400} and Cu@C_{600}, many larger pores were found in Cu@C_{800}, and these inhomogeneously nanosized pores should be beneficial in providing

Table 1 Surface area, pore volumes and pore sizes for the precursor and five resultant Cu@C samples

Samples	S_L[a] (m^2 g^{-1})	S_{BET}[b] (m^2 g^{-1})	V_{total}[c] (cm^3 g^{-1})	V_{micro}[d] (cm^3 g^{-1})	$V_{meso+macro}$[e] (cm^3 g^{-1})	D_c[f] (nm)
Cu@C_{400}	152.1	100.9	0.10	0.03	0.08	11.013
Cu@C_{600}	281.7	190.6	0.14	0.087	0.06	14.969
Cu@C_{800}	204.5	138.8	0.08	0.068	0.03	32.18
Cu@$C_{800\text{-}2H}$	186.8	124.3	0.07	0.065	0.04	78.12
Cu@$C_{800\text{-}8H}$	268.5	182.1	0.14	0.087	0.11	41.72

[a] Calculated from Langmuir surface area. [b] Calculated from BET surface area. [c] The pore volume is calculated at a relative pressure of 0.98. [d] *t*-Plot micropore volume. [e] Meso- and macropore volumes are determined by subtracting the micropore volume from the total pore volume. [f] The average pore diameter calculated from the adsorption curve by the BJH method.

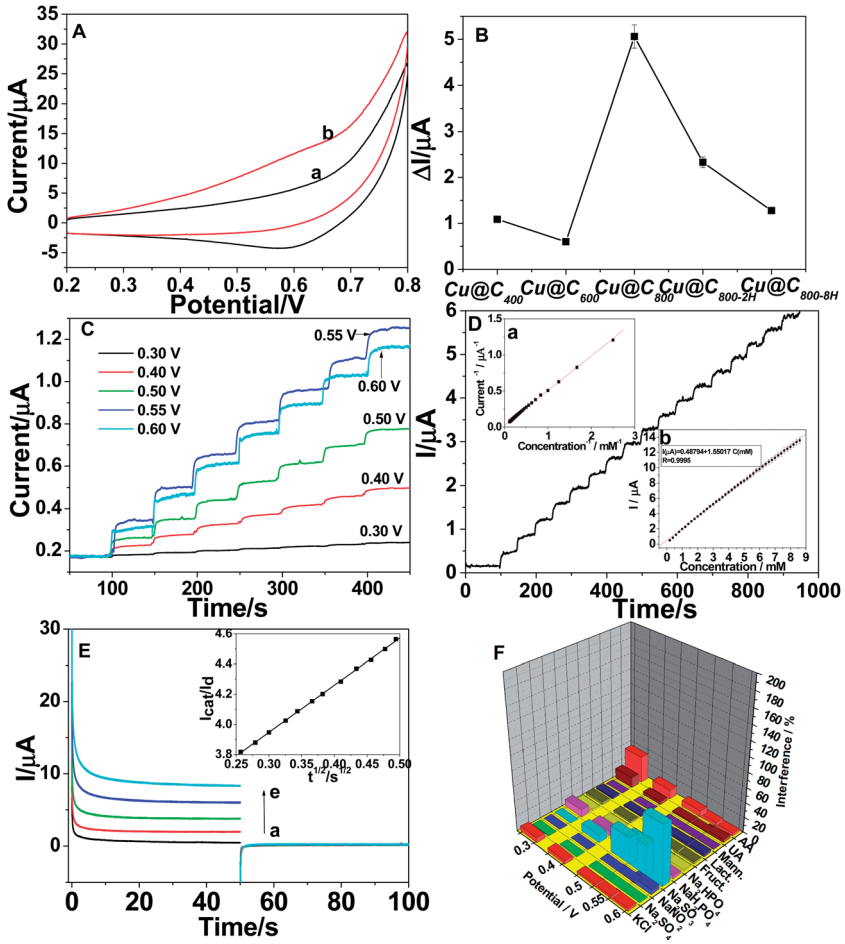

Fig. 6 (A) CVs of the Cu@C_{800} modified electrode in the absence (a) and presence (b) of 1.0 mM glucose in 0.1 M NaOH solution at a scan rate of 100 mV s^{-1}. (B) Plot of catalytic oxidation peak current of different modified electrodes based on Cu@C nanocomposites towards 1.0 mM glucose in 0.1 M NaOH at a scan rate of 100 mV s^{-1}. (C) Amperometric responses of the Cu@C_{800} modified electrode at different potentials in 0.1 M NaOH with a 5 μL addition of 0.1 mM glucose. (D) Amperometric responses at +0.55 V with an increasing glucose concentration of 0.2 mM per 50 s for the Cu@C_{800} modified electrode. Inset a: calibration curve obtained at the Cu@C_{800} modified electrode. Inset b: Lineweaver–Burk plot. (E) Chronoamperograms of the Cu@C_{800} modified electrode in 0.1 M NaOH solution containing (a) 0, (b) 2, (c) 4, (d) 6 and (e) 8 mM glucose. Inset: plot of I_{cat}/I_d *versus* $t_{1/2}$ for 6.0 mM glucose. (F) Interference test of the sensor in 0.1 M NaOH at different potentials with 2.0 mM glucose and other interferents as indicated.

space and sites for the electrolyte and glucose transfer. When the temperature was maintained at 800 °C, Cu nanoclusters were further agglomerated and resulted in poor catalytic activity of Cu@$C_{800\text{-}2H}$ and Cu@$C_{800\text{-}8H}$.

A credible mechanism of the electrocatalytic oxidation of glucose in alkaline solution by metallic Cu nanoclusters was proposed by Marioli and Kuwana.[30] An important step in the oxidation of carbohydrates involves the interaction between the carbohydrates and the Cu(III) oxide/hydroxide layer covering the electrode. After the adsorption step, the Cu(III) further oxidizes the carbohydrate through C–C bond cleavage, and the possible redox mechanism could be assumed as followed:[2]

$$CuOOH + \text{glucose} \rightarrow Cu(OH)_2 + H_2O + \text{glucosone} \quad (3)$$

In this work, small Cu nanoclusters and the porous carbon framework might increase the specific surface area and thus enhance electrocatalytic activity.

It is well known that the sensitivity of electrochemical biosensors is strongly dependent on the applied potential. To study the effect of the working potential on the electrocatalytic oxidation of glucose at the Cu@C_{800} modified electrode, the amperometric responses to seven successive injections of 0.1 mM glucose were recorded at different applied potentials varying from 0.30 to 0.60 V, as shown in Fig. 6C. The current response increased as the working potential increased, reaching the maximal value at 0.55 V. Thus, 0.55 V was chosen as the working potential in the following amperometric measurements to investigate the linear range of the modified electrode by successive injection of glucose into a stirred 0.1 M NaOH solution (Fig. 6D). It was noticeable that the noise increased with increasing glucose concentration. It might be because more and more intermediate species adsorbed onto the modified electrode as the glucose concentration and the reaction time increased. The current response presented a linear dependence upon the

concentration of glucose (I (μA) = 0.48794 + 1.55017C, R = 0.9995) in the range of 0.2–8.0 mM. The detection limit was estimated to be 29.8 μM, based on the criterion of a signal-to-noise ratio of 3 ($S/N = 3$). The K_M^{app} was also calculated to be 0.05 mM according to the Lineweaver–Burk plot (inset b in Fig. 6D).[31] The smaller value indicated a higher catalytic activity compared with previously reported results and some glucose oxidase electrodes.[32–34]

Furthermore, chronoamperometry was used for the evaluation of the catalytic rate constant K_{cat} by setting the working electrode potentials to appropriate values.[35] Fig. 6E showed double potential step chronoamperograms for the Cu@C_{800} modified electrode in the absence (curve a) and presence (curve b: 2.0 mM, curve c: 4.0 mM, curve d: 6.0 mM and curve e: 8.0 mM) of glucose. The applied potential steps were set to 0.55 V and 0.20 V, respectively. In the following equation:

$$\frac{I_{cat}}{I_d} = \lambda^{1/2}\left[\pi^{1/2}\mathrm{erf}\left(\lambda^{1/2}\right) + \frac{\exp(-\lambda)}{\lambda^{1/2}}\right] \quad (4)$$

where I_{cat} and I_d were the currents in the presence and absence of glucose, $\lambda = K_{cat}Ct$ was the argument of the error function, K_{cat} was the catalytic rate constant and t was the consumed time. In cases where $\lambda > 1.5$, erf($\lambda^{1/2}$) was almost equal to unity, and the above equation could be reduced to:

$$\frac{I_{cat}}{I_d} = \lambda^{1/2}\pi^{1/2} = \pi^{1/2}(K_{cat}Ct)^{1/2} \quad (5)$$

From the slope of the I_{cat}/I_d *versus* $t^{1/2}$ plot, as shown in inset of Fig. 6E, the mean value of K_{cat} for glucose was calculated to be 15.54×10^6 cm^3 mol^{-1} s^{-1}. All of the kinetic parameters obtained in this work were summarized in Table 2. Although many glucose sensors based on Cu materials with various shapes have been developed, all of these sensors have their own advantages and limitations.[36] Generally, the detection limits are fairly low, and the linear ranges are relatively narrow. Some studies, such as those involving Cu/Cu_2O hollow spheres,[13] have obtained excellent results by incorporating Cu_xO and increasing the amount of active material. However, the sensor based on HKUST-1-derived anthill-like Cu@carbon nanocomposites in this work shows an advance to some extent due to its simple preparation, wider linear range and sufficiently low detection limit for routine inspection.

Since interference is inevitable in the determination of some analytes, several common inorganic ions and organic molecules were investigated at different potentials. Considering the concentration of glucose is at least 30 times that of interfering species in human blood, the interference tests were carried out by adding 2.0 mM glucose, followed by additions of 2.0 mM inorganic salts and organic molecules. As shown in Fig. 6F, at 0.55 V, these species presented little interference. At an applied potential of 0.3 V, the catalytic current towards glucose was so low that the small current from the interferents became prominent. At 0.6 V, the catalytic current towards glucose was relatively high, but the high potential caused a 78.9% response current of Na_2SO_3. Therefore, 0.55 V was selected as the optimized operating potential to fulfill the selectivity and sensitivity requirements of the present biosensor. Long-term stability of the sensor was examined by measuring its current response to glucose over 10 days. Only 7% loss in the current signal was observed, indicating good stability of the sensor.

4. Conclusion

In summary, a novel HKUST-1-derived anthill-like Cu@carbon nanocomposite was introduced for the first time for the construction of a nonenzymatic glucose sensor, which involved only low-cost raw materials and a simple thermolysis process. The derived material consisted of Cu nanoclusters embedded in a porous carbon framework, and exhibited a large specific surface area and high electrocatalytic activity towards glucose. With a relatively wide linear range and low limit of detection, this material could be a potential candidate for routine glucose analysis.

Acknowledgements

This work was financially supported by the National Natural Science Foundation of China (21065005, 21305054 and 21101146), the Young Scientist Foundation of Jiangxi Province (20112BCB23006), the State Key Laboratory of Electroanalytical Chemistry (SKLEAC201310), and the Open Project Program of Key Laboratory of Functional Small Organic Molecules, Ministry of Education, Jiangxi Normal University (no. KLFS-KF-201214).

Table 2 Comparison of the performance of the Cu@C_{800} modified electrode with other glucose sensors based on different Cu materials

	Detection potential (V)	K_{cat} (cm^3 mol^{-1} s^{-1})	Detection limit (μmol L^{-1})	Linear range (mmol L^{-1})	Reference
Cu@C_{800}	0.55 (*vs.* SCE)	15.54×10^6	29.8	0.2–8.0	This work
Cu/graphene	0.5 (*vs.* SCE)	—	5	Up to 4.5	14
Cu–TiO_2/glucose oxidase	0.6 (*vs.* SCE)	—	0.1	0.0005–3.0	37
Cu MWs–MWCNTs	0.55 (*vs.* Ag/AgCl)	—	0.26	Up to 3.0	38
Cu/Cu_2O hollow microspheres	0.45 (*vs.* SCE)	—	0.05	0.22–10.89	13
Cu–MWCNTs	0.63 (*vs.* SCE)	—	2	0.5–7.5	39
CuO–SWCNT	0.45 (*vs.* SCE)	—	0.05	0.00005 to 1.8	40
CuO–G–GCE	0.55 (*vs.* SCE)	—	0.7	0.002–4	41

References

1 A. Heller and B. Feldman, *Chem. Rev.*, 2008, **108**, 2482–2505.
2 K. E. Toghill and R. G. Compton, *Int. J. Electrochem. Sci.*, 2010, **5**, 1246–1301.
3 J. Wang, *Chem. Rev.*, 2008, **108**, 814–825.
4 O. Yehezkeli, R. Tel-Vered, S. Raichlin and I. Willner, *ACS Nano*, 2011, **5**, 2385–2391.
5 W. Lu, X. Qin, A. M. Asiri, A. O. AlYoubi and X. Sun, *Analyst*, 2013, **138**, 417–420.
6 J. Tian, Q. Liu, A. M. Asiri, A. Qusti, A. Alyoubi and X. Sun, *Nanoscale*, 2013, **5**, 8921–8924.
7 X. Lu, X. Xiao, Z. Li, F. Xu, H. Tan, L. Sun and L. Wang, *Anal. Methods*, 2014, **6**, 235–241.
8 Y. Zhang, X. Xiao, Y. Sun, Y. Shi, H. Dai, P. Ni, J. Hu, Z. Li, Y. Song and L. Wang, *Electroanalysis*, 2013, **25**, 959–966.
9 H. Liu, X. Lu, D. Xiao, M. Zhou, D. Xu, L. Sun and Y. Song, *Anal. Methods*, 2013, **5**, 6360–6367.
10 L. Wang, X. Lu, Y. Ye, L. Sun and Y. Song, *Electrochim. Acta*, 2013, **114**, 484–493.
11 S. Liu, J. Tian, L. Wang, X. Qin, Y. Zhang, Y. Luo, A. M. Asiri, A. O. Al-Youbi and X. Sun, *Catal. Sci. Technol.*, 2012, **2**, 813–817.
12 J. Liu and D. Xue, *J. Mater. Chem.*, 2011, **21**, 223–228.
13 A. J. Wang, J. J. Feng, Z. H. Li, Q. C. Liao, Z. Z. Wang and J. R. Chen, *CrystEngComm*, 2012, **14**, 1289–1295.
14 J. Luo, S. Jiang, H. Zhang, J. Jiang and X. Liu, *Anal. Chim. Acta*, 2012, **709**, 47–53.
15 A. P. Periasamy, J. Liu, H.-M. Lin and H.-T. Chang, *J. Mater. Chem. A*, 2013, **1**, 5973–5981.
16 L. C. Jiang and W. D. Zhang, *Biosens. Bioelectron.*, 2010, **25**, 1402–1407.
17 A. Dhakshinamoorthy and H. Garcia, *Chem. Soc. Rev.*, 2012, **41**, 5262–5284.
18 V. Lykourinou, Y. Chen, X. S. Wang, L. Meng, T. Hoang, L. J. Ming, R. L. Musselman and S. Ma, *J. Am. Chem. Soc.*, 2011, **133**, 10382–10385.
19 N. Stock and S. Biswas, *Chem. Rev.*, 2012, **112**, 933–969.
20 H. L. Jiang, B. Liu, Y. Q. Lan, K. Kuratani, T. Akita, H. Shioyama, F. Zong and Q. Xu, *J. Am. Chem. Soc.*, 2011, **133**, 11854–11857.
21 R. Das, P. Pachfule, R. Banerjee and P. Poddar, *Nanoscale*, 2012, **4**, 591–599.
22 B. Liu, H. Shioyama, T. Akita and Q. Xu, *J. Am. Chem. Soc.*, 2008, **130**, 5390–5391.
23 S. S. Chui, *Science*, 1999, **283**, 1148–1150.
24 K. Schlichte, T. Kratzke and S. Kaskel, *Microporous Mesoporous Mater.*, 2004, **73**, 81–88.
25 Y. K. Seo, G. Hundal, I. T. Jang, Y. K. Hwang, C. H. Jun and J. S. Chang, *Microporous Mesoporous Mater.*, 2009, **119**, 331–337.
26 Z. Q. Li, L. G. Qiu, T. Xu, Y. Wu, W. Wang, Z.-Y. Wu and X. Jiang, *Mater. Lett.*, 2009, **63**, 78–80.
27 R. Ameloot, L. Stappers, J. Fransaer, L. Alaerts, B. F. Sels and D. E. De Vos, *Chem. Mater.*, 2009, **21**, 2580–2582.
28 P. L. Feng, J. J. t. Perry, S. Nikodemski, B. W. Jacobs, S. T. Meek and M. D. Allendorf, *J. Am. Chem. Soc.*, 2010, **132**, 15487–15489.
29 S. J. Yang, T. Kim, J. H. Im, Y. S. Kim, K. Lee, H. Jung and C. R. Park, *Chem. Mater.*, 2012, **24**, 464–470.
30 J. M. Marioli and T. Kuwana, *Electrochim. Acta*, 1992, **37**, 1187–1197.
31 Y. Dong, H. Zhang, Z. Rahman, L. Su, X. Chen, J. Hu and X. Chen, *Nanoscale*, 2012, **4**, 3969–3976.
32 Z. Wang, S. Liu, P. Wu and C. Cai, *Anal. Chem.*, 2009, **81**, 1638–1645.
33 Ch. Wu, X. Liu, Y. Li, X. Du, X. Wang and P. Xu, *Biosens. Bioelectron.*, 2014, **53**, 26–30.
34 M. B. Gholivand and M. Khodadadian, *Biosens. Bioelectron.*, 2014, **53**, 472–478.
35 Y. Song, Z. He, H. Hou, X. Wang and L. Wang, *Electrochim. Acta*, 2012, **71**, 58–65.
36 L. Wang, J. Fu, H. Hou and Y. Song, *Int. J. Electrochem. Sci.*, 2012, **7**, 12587–12600.
37 X. Zhang, G. Wang, Y. Huang, L. Yu and B. Fang, *Anal. Methods*, 2011, **3**, 2611–2615.
38 J. Huang, Z. Dong, Y. Li, J. Li, J. Wang, H. Yang, S. Li, S. Guo, J. Jin and R. Li, *Semin. Cell Dev. Biol.*, 2013, **182**, 618–624.
39 J. Zhao, L. Wei, C. Peng, Y. Su, Z. Yang, L. Zhang, H. Wei and Y. Zhang, *Biosens. Bioelectron.*, 2013, **47**, 86–91.
40 N. Dung, D. Patil, H. Jung and D. Kim, *Biosens. Bioelectron.*, 2013, **42**, 280–286.
41 L. Luo, L. Zhu and Z. Wang, *Bioelectrochemistry*, 2012, **88**, 156–163.